AIAA 94–0056

Fully-Implicit Time-Marching Aeroelastic Solutions

Juan J. Alonso and Antony Jameson
Princeton University, Princeton, NJ 08544

32nd AIAA Aerospace Sciences Meeting and Exhibit
January 10–13, 1994/Reno, NV

Fully-Implicit Time-Marching Aeroelastic Solutions

Juan J. Alonso[*] and Antony Jameson[†]
Princeton University, Princeton, NJ 08544

A new fully-implicit approach for computing transonic aeroelastic solutions is presented. The unsteady Euler equations are coupled with a typical section swept wing model and integrated forward in time. The implicit Euler equations are integrated in pseudo-time using multigrid methods, and are coupled with a first-order system decomposition of the structural modal equations. Full convergence of the simultaneous governing equations is achieved at every time step with considerable computational savings over previous approaches. Transient responses for a NACA 64A010 are calculated in different flow regimes, and flutter boundaries are computed and compared to pre-existing numerical data.

Nomenclature

a non-dimensional location of the elastic axis, positive aft of midchord

b airfoil semichord

c airfoil chord

C_l coefficient of lift

C_m coefficient of moment about the elastic axis, positive nose up

E total energy (internal plus kinetic)

$\mathbf{f}, \mathbf{g}$ Euler flux vectors

h plunging displacement of the elastic axis, positive down

H total enthalpy

I_α section moment of inertia about the elastic axis, $I_\alpha = mb^2 r_\alpha^2$

J jacobian of the transformation from cartesian to body fitted coordinates

k_c reduced frequency, $k_c = \frac{\omega c}{U_\infty}$

K_h plunging spring constant

K_α pitching spring constant

L airfoil section lift (normal to free stream), positive up

m airfoil mass per unit span

M_{ea} total moment about the elastic axis, positive nose up

M_∞ free stream Mach number

$\vec{n}$ surface normal vector

p static pressure

Q_i generalized force for ith mode

$\mathbf{R}(\mathbf{w}_{ij})$ flux residual for cell i,j

$\mathbf{R}^*$ modified residual

R_{ij}^* modified residuals for structural equations

S_α static unbalance, positive for c.g. aft of midchord, $S_\alpha = mbx_\alpha$

t real time

t^* pseudo-time

u, v cartesian velocity components

$\vec{u}$ cartesian velocity vector

U_∞ free stream velocity

U_f flutter speed

V_{ij} volume of i,j cell

V_f flutter speed index, $V_f = \frac{U_f}{b\omega_\alpha \sqrt{\mu}}$

$\mathbf{w}$ vector of flow variables

x_t, y_t mesh cartesian velocity components

x_{ij}, z_{ij} first order system decomposition intermediate variables

α angle of attack, in radians

$\Delta\alpha$ pitching motion forcing amplitude

Δt implicit real time step

γ ratio of specific heats, $\gamma = 1.4$

η_i ith normal coordinate

μ airfoil mass ratio, $\mu = \frac{m}{\pi\rho b^2}$

ρ air density

ω_f frequency of the forced oscillations

ω_h, ω_α uncoupled natural frequencies of typical section in plunge and pitch respectively

ω_i coupled natural frequency of the ith mode

$\Omega, \partial\Omega$ cell element and boundary

τ non-dimensional structural time, $\tau = \omega_\alpha t$

ζ_i modal damping of the ith mode

$\{F\}$ forcing vector

$[K]$ stiffness matrix

$[M]$ mass matrix

$[P_i]$ transformation matrix for the ith modal equation decomposition

$[\phi]$ mass normalized eigenvector matrix

$\{q\}$ displacement vector

---

[*]Graduate Student, AIAA Member

[†]James S. McDonnell Distinguished University Professor of Aerospace Engineering, AIAA Fellow

Introduction

TRANSONIC aeroelasticity is a topic of current research interest because of the essential role it plays in aircraft design. Modern aircraft tend to possess a high level of flexibility in order to satisfy low

weight and maneuverability requirements. As a result, there is the possibility that several aeroelastic phenomena occur which severely limit the flight envelope and performance. Well known examples are the initial flight tests of the B-1 wing and the wind tunnel testing of the HiMAT canard model.[1]

The transonic regime presents additional difficulties to the solution of the aeroelastic problem. In the subsonic and supersonic flow regimes, it is normal practice to linearize the fluid flow equations such that the forces and moments acting on the aerodynamic configuration depend only linearly on the motion of the airfoil. These aerodynamic models can be coupled with the linearized structural equations of motion to produce reasonably accurate results. Unfortunately, the highly non-linear nature of the transonic regime results in large variations of the forces and moments with small changes of the aerodynamic configuration. This non-linearity prohibits the decoupling of the structural and flow equations. Thus, numerical solution of the full set of non-linear equations must be used in order to obtain meaningful results.

In the past, aeroelastic predictions from the supersonic and subsonic regions have been extrapolated to the transonic regime. Isogai[2,3] showed the existence of a sharp decrease in the flutter speed of a swept wing in transonic flight ($M_\infty \approx 0.7 - 0.9$) . This "transonic dip" phenomenon can only be predicted by including the flow equation non-linearities in the model. When subsonic linear theories are extended into the transonic regime, the flutter point is severely overpredicted, leading to very dangerous design conclusions.

The first attempts to obtain time-marching solutions of two-dimensional aeroelastic configurations used the transonic small disturbance (TSD) equation to model the unsteady behavior of the flow. The LTRAN2S computer program[4] was used to investigate the response of a NACA 64A010 airfoil in the low reduced frequency range ($k_c \approx 0.075 - 0.1$). The XTRAN3S computer code[5] used a similar approach and modeled the behavior of three-dimensional wings. Edwards *et al.*[6] used a monotone differencing method in order to eliminate expansion shocks in the neighborhood of the leading edge of the airfoil and extended the validity of the solution into the higher reduced frequency range ($k_c \approx 0.3 - 0.4$). These methods give a reasonable prediction of the flutter boundary for a given airfoil.

The "transonic dip" phenomenon has been traced back to the large negative value of the out-of-phase component of the load distribution caused by the phase lag of the shock wave motion.[7] Furthermore, Farmer and Hanson[8] obtained experimental data which showed the marked influence of the thickness distribution of the airfoil on the unsteady characteristics of the aerodynamic loading. Therefore, we need a flow model that can both accurately predict the phase lag in the motion of the shock waves on the upper and lower surfaces of the airfoil and impose the correct boundary conditions in order to account for thickness effects adequately. The TSD equation is unable to meet these two requirements properly and therefore, a more refined aerodynamic model is necessary.

The large improvement in computing resources in the last decade, tied with advances in computational methods, has motivated the appearance of aeroelastic codes that employ the Euler equations as a fluid flow model. Bendiksen and Kousen[9,10] first used an explicit aerodynamic code coupled with a structural integrator based on the convolution integral to obtain the flutter boundary for a NACA 64A010 airfoil. In the process they discovered the existence of large amplitude limit cycles in the motion of the system.[11] Guruswamy[12,13] has reported some very encouraging results with Euler and Navier-Stokes equations for two- and three-dimensional configurations including vortical flows.

In spite of the recent advances, aeroelastic calculations using these refined aerodynamic models remain very computationally expensive. In addition to this problem, the two sets of equations (fluid flow and structural model) are treated separately and integrated in a "leap-frog" fashion with the result that we never have a fully converged system at any one time step.

Jameson[14] has developed a very efficient multigrid-driven implicit approach to the solution of the unsteady Euler equations. Using central differences in space and an implicit multistep discretization in time, a large set of simultaneous non-linear equations is formed and marched to steady-state in pseudo-time through a multigrid algorithm within each real time step. This approach has been recently applied to the solution of the unsteady Navier-Stokes equations with great promise.[17,18]

This paper describes the full coupling of the Euler equations with the typical section wing model used in the code UFLO82S (a derivative of Jameson's UFLO82 code[14]). The flow equations are implicitly solved using Jameson's algorithm and each of the modal equations of motion of the structure is decomposed into a set of first-order ordinary differential equations. This set of equations is then marched in time with an implicit linear multistep method. The system (fluid flow and structural model) is fully coupled and a fully converged solution is achieved at every time step of the calculation with very substantial computational savings. The code is used to produce flutter boundaries for a NACA 64A010 airfoil using the Isogai swept wing model structural parameters.

Governing Aerodynamic Equations

The governing equations of the flow are the Euler equations. Let p, ρ, u, v, H, and E denote the pressure, density, cartesian velocity components, total enthalpy, and total energy respectively. Consider a control volume Ω with boundary $\partial\Omega$ which moves with cartesian velocity components x_t and y_t. The equations of motion of the fluid can then be written in integral form as

$$\frac{d}{dt}\iint_{\Omega} \mathbf{w}\, dx\, dy + \oint_{\partial\Omega} (\mathbf{f}\, dy - \mathbf{g}\, dx) = \mathbf{0}, \quad (1)$$

where $\mathbf{w}$ is the vector of flow variables

$$\mathbf{w} = \left\{ \begin{array}{c} \rho \\ \rho u \\ \rho v \\ \rho E \end{array} \right\},$$

and $\mathbf{f}$, $\mathbf{g}$ are the Euler flux vectors

$$\mathbf{f} = \left\{ \begin{array}{c} \rho(u - x_t) \\ \rho u(u - x_t) + p \\ \rho v(u - x_t) \\ \rho E(u - x_t) + pu \end{array} \right\}, \; \mathbf{g} = \left\{ \begin{array}{c} \rho(v - y_t) \\ \rho u(v - y_t) \\ \rho v(v - y_t) + p \\ \rho E(v - y_t) + pv \end{array} \right\}.$$

Also, for an ideal gas, the equation of state may be written as

$$p = (\gamma - 1)\, \rho\, \left[E - \frac{1}{2}(u^2 + v^2) \right].$$

Applying Equation 1 independently to each cell in the mesh we obtain a set of ordinary differential equations of the form

$$\frac{d}{dt}(\mathbf{w}_{ij}\, V_{ij}) + \mathbf{R}(\mathbf{w}_{ij}) = \mathbf{0}, \quad (2)$$

where V_{ij} is the volume of the i, j cell and the residual $\mathbf{R}(\mathbf{w}_{ij})$ is obtained by evaluating the flux integral in Equation 1. Following Jameson,[14] in order to prevent oscillations in the neighborhood of shock waves and to provide background dissipation to suppress odd-even modes, a blend of first- and third-order dissipative fluxes is added. These dissipative terms provide an upwind bias and are added in the form of dissipative fluxes for conservation purposes.

In order to obtain a fully-implicit algorithm, approximate Equation 2 as follows (drop the subscripts i, j for clarity):

$$\frac{d}{dt}[\mathbf{w}^{n+1}\, V^{n+1}] + \mathbf{R}(\mathbf{w}^{n+1}) = \mathbf{0}, \quad (3)$$

where the superscript $n+1$ denotes the time level $(n+1)\Delta t$. The $\frac{d}{dt}$ operator is approximated by an implicit backwards difference formula of kth-order accuracy of the form

$$\frac{d}{dt} = \frac{1}{\Delta t}\sum_{q=1}^{k} \frac{1}{q}\left[\Delta^{-}\right]^q, \quad (4)$$

where

$$\Delta^{-} = \mathbf{w}^{n+1} - \mathbf{w}^n.$$

The baseline version of the code uses a second-order accurate operator, which casts Equation 3 in the following form

$$\frac{3}{2\Delta t}[\mathbf{w}^{n+1}V^{n+1}] - \frac{2}{\Delta t}[\mathbf{w}^n V^n] + \frac{1}{2\Delta t}[\mathbf{w}^{n-1}V^{n-1}]$$
$$+ \mathbf{R}(\mathbf{w}^{n+1}) = \mathbf{0}. \quad (5)$$

This time discretization is A-Stable[15] when applied to the test linear differential equation

$$\frac{dw}{dt} = \alpha\, w.$$

The third-order accurate backwards difference (obtained with $k = 3$ in Equation 4) has been defined as stiffly stable by Gear.[16] Its stability region is slightly more restrictive and could, in principle, present some difficulties for the Euler equations since the model problems require stability along the imaginary axis. However, as we will show in the results section, the third-order accurate algorithm has proven to be robust for the Euler equations. Recently, Melson *et al.*[17] have shown conditional stability for the fourth-order accurate algorithm with a slightly different treatment of the multigrid terms. Nevertheless, the bulk of the results contained in this paper were obtained with the second-order accurate time discretization.

Equation 5 represents an implicit set of coupled ordinary differential equations. These equations can be solved at each time step using the same multistage techniques for explicit steady-state calculations if we define the modified residual $\mathbf{R}^*(\mathbf{w})$ as

$$\mathbf{R}^*(\mathbf{w}) = \frac{3}{2\Delta t}[\mathbf{w}\, V^{n+1}]$$
$$- \frac{2}{\Delta t}[\mathbf{w}^n V^n] + \frac{1}{2\Delta t}[\mathbf{w}^{n-1}V^{n-1}] + \mathbf{R}(\mathbf{w}),$$

and march to steady-state in a fictitious time, t^*, the following ordinary differential equation

$$\frac{d\mathbf{w}}{dt^*} + \mathbf{R}^*(\mathbf{w}) = \mathbf{0}. \quad (6)$$

Within each real time step, the set of ordinary differential Equations 6 is solved using a five-stage Runge-Kutta scheme. In order to accelerate convergence, a multigrid strategy is employed. In addition, residual averaging and local time stepping are also used. Notice that enthalpy damping must be disabled since an unsteady flow does not admit a constant enthalpy solution. Details of these procedures are contained in[14] and.[19] Note that since the two-dimensional calculations in this work used an O-mesh rigidly attached to the airfoil, the cell volumes are constant and can therefore be factored out. Due to this fact no regridding is necessary; the grid is rotated and translated in a rigid body motion fashion after each time step.

Boundary Conditions

At the airfoil surface, the flow tangency boundary condition needs to be imposed. This is easily achieved by eliminating the convective fluxes across the edges of the mesh which lie directly on the surface of the airfoil. The fluxes for the x- and y-momentum equations have a component due to the integral of the pressure along the surface of the airfoil. Since the flow solver is based on a cell centered discretization of the governing equations, the value of the pressure at the airfoil surface is not readily available and we must find a way to calculate it from the information inside of the domain. This estimate of the pressure can be obtained by either extrapolating from the values of adjacent cells or by use of a discretized form of the normal momentum equation.

The second approach has proven to yield better results in two-dimensional steady-state solvers, and thus, following Rizzi,[20] the derivative of the pressure in the normal direction to the solid wall is computed from the unsteady momentum equations. Streamline differentiation of the wall boundary condition, $(\vec{u} \cdot \vec{n}) = 0$, together with the unsteady momentum equation dotted with the unit normal, $\vec{n}$, yields the following relationship

$$\rho \vec{u} \cdot \left(\frac{\partial}{\partial t} + \vec{u} \cdot \boldsymbol{\nabla} \right) \vec{n} = \vec{n} \cdot \boldsymbol{\nabla} p \qquad (7)$$

We now construct a transformation from cartesian coordinates $(x, y; t)$ to body conforming coordinates $(X, Y; \tau)$, where X is along the surface of the airfoil and Y is normal to it. This transformation is defined by its jacobian $J = \frac{\partial(x,y,t)}{\partial(X,Y,\tau)}$. Substitution of the normal vector $\vec{n}$ by its components $(\frac{y_X}{|\vec{n}|}, \frac{-x_X}{|\vec{n}|})$ into Equation 7 yields the following expression for the normal pressure gradient, p_Y, at the airfoil surface:

$$(x_X^2 + y_X^2) \, p_Y = (x_X \, x_Y + y_X \, y_Y) p_X$$
$$+ \rho(y_Y \, u - x_Y \, v - J x_t)(v \, x_{XX} - u \, y_{XX})$$
$$+ \rho \, J \, y_t (u \, y_{XY} - v \, x_{XY}) - \rho \, J \, (u \, y_{X\tau} - v \, x_{X\tau})$$

where the time derivatives of the metrics are computed using the backwards difference operator of Equation 4.

In the far field, non-reflecting boundary conditions are applied based on the work of Venkatakrishnan,[21] although a more refined far field model is under study.

Aeroelastic Model

The typical section wing model[22, 23] is by now a well established two-dimensional analog of a three-dimensional wing. This model (see Figure 1) features two degrees of freedom, which we shall refer to as pitching and plunging degrees of freedom. The governing equations of motion can be shown to be

$$m\ddot{h} + S_\alpha \ddot{\alpha} + K_h h = -L$$
$$S_\alpha \ddot{h} + I_\alpha \ddot{\alpha} + K_\alpha \alpha = M_{ea},$$

where L and M_{ea} are the lift (positive up) and moment about the elastic axis (positive nose up), K_h and K_α are bending and torsional spring stiffnesses, and h and α are the plunging coordinate (positive down) and the angle of attack (in radians). Non-dimensionalizing time by the uncoupled natural frequency of the torsional spring, $\tau = \omega_\alpha t$, we can rewrite the equations of motion in the more familiar form

$$[M]\{\ddot{q}\} + [K]\{q\} = \{F\}, \qquad (8)$$

where

$$[M] = \begin{bmatrix} 1 & x_\alpha \\ x_\alpha & r_\alpha^2 \end{bmatrix}, \quad [K] = \begin{bmatrix} \left(\frac{\omega_h}{\omega_\alpha}\right)^2 & 0 \\ 0 & r_\alpha^2 \end{bmatrix}$$

are the non-dimensional mass and stiffness matrices, and

$$[F] = \frac{4}{\pi \mu k_c^2} \begin{bmatrix} -C_l \\ 2C_m \end{bmatrix}, \qquad \{q\} = \left\{ \begin{array}{c} \frac{h}{b} \\ \alpha \end{array} \right\},$$

are the load and displacement vectors. C_l and C_m are the coefficient of lift and the coefficient of moment about the elastic axis. In order to solve Equation 8, a Rayleigh-Ritz modal approach is used. The mode shapes and frequencies are obtained by solving the generalized eigenproblem[24] associated with the free vibration problem and, in general, only the first N modes are considered. With these first N modes we have an approximate description of the displacement vector of the system given by

$$\{q\} = \sum_{r=1}^{N} \eta_r \{\phi\}_r,$$

where $\{\phi\}_r$ is the rth eigenvector of the generalized eigenproblem, and η_r is the corresponding normal coordinate. This truncated representation yields a valid model if the modal frequencies of the ignored mode shapes are much higher than the values of the aerodynamic frequencies involved in the problem. In our case, for a two degree-of-freedom problem, we have only two eigenfrequencies corresponding to the two eigenmodes (symmetric and antisymmetric) which span the whole space. Therefore, no truncation is needed. On the other hand, in the three-dimensional version of the code, only the N lower frequency modes are kept yielding a truncated model in which the displacement vector is restricted to lie in the subspace spanned by these N eigenmodes. The displacement vector can then be decomposed as

$$\{q\} = [\phi]\{\eta\}.$$

Since the eigenvectors are orthogonal with respect to both the mass and stiffness matrices, premultiplying Equation 8 by $[\phi]^T$ (normalized such that the eigenvectors are orthonormal with respect to the mass matrix)

yields a set of equations in generalized coordinates of the form

$$\ddot{\eta}_i + 2\zeta_i\omega_i\dot{\eta}_i + \omega_i^2\eta_i = Q_i, \quad i = 1, 2 \qquad (9)$$

where

$$
\begin{aligned}
Q_i &= \{\phi\}_i^T\{F\} \\
\omega_i^2 &= \{\phi\}_i^T[K]\{\phi\}_i \\
1 &= \{\phi\}_i^T[M]\{\phi\}_i,
\end{aligned}
$$

and ζ_i is the modal damping of the ith mode that has been added to the model. The assumption of the existence of a modal damping parameter supposes that the damping matrix (which is not included in Equation 8) is diagonalized by the appropriate pre- and post-multiplication by $[\phi]^T$ and $[\phi]$.

The structural integrator is based on the decomposition of each of the modal Equations (9) into a system of first-order differential equations. Using the transformation

$$
\begin{aligned}
x_{1i} &= \eta_i \\
\dot{x}_{1i} &= x_{2i} \\
\dot{x}_{2i} &= Q_i - 2\zeta_i\omega_i x_{2i} - \omega_i^2 x_{1i}
\end{aligned}
$$

for each of the modal equations, we can rewrite Equations 9 in matrix form as

$$\{\dot{X}_i\} = [A_i]\{X_i\} + \{F_i\}, \quad i = 1, 2$$

where

$$\{X_i\} = \left\{ \begin{array}{c} x_{1i} \\ x_{2i} \end{array} \right\}, \quad [A_i] = \left[\begin{array}{cc} 0 & 1 \\ -\omega_i^2 & -2\omega_i\zeta_i \end{array} \right],$$

and

$$\{F_i\} = \left\{ \begin{array}{c} 0 \\ Q_i \end{array} \right\}.$$

Now, for this system, assume another transformation $\{X_i\} = [P_i]\{Z_i\}$, such that the new system

$$\{\dot{Z}_i\} = ([P_i]^{-1}[A_i][P_i])\{Z_i\} + [P_i]^{-1}\{F_i\}$$

is decoupled. That is, the matrices $([P_i]^{-1}[A_i][P_i])$ are diagonal. Then for each mode, the governing equations of the motion of the structure are

$$
\begin{aligned}
\frac{dz_{1i}}{dt} &= \omega_i(-\zeta_i + \sqrt{\zeta_i^2 - 1})\,z_{1i} + \frac{(-\zeta_i + \sqrt{\zeta_i^2 - 1})}{2\sqrt{\zeta_i^2 - 1}}\,Q_i \\
\frac{dz_{2i}}{dt} &= \omega_i(-\zeta_i - \sqrt{\zeta_i^2 - 1})\,z_{2i} + \frac{(\zeta_i + \sqrt{\zeta_i^2 - 1})}{2\sqrt{\zeta_i^2 - 1}}\,Q_i.
\end{aligned}
$$

In these equations, the time derivative operator can be discretized as in Equation 5 for second-, third-, or higher-order accuracy. For second order accuracy the result is the following set of two difference equations for each mode

$$\frac{3z_{1i}^{n+1} - 4z_{1i}^n + z_{1i}^{n-1}}{2\Delta t} =$$

$$\omega_i(-\zeta_i + \sqrt{\zeta_i^2 - 1})\,z_{1i}^{n+1} + \frac{(-\zeta_i + \sqrt{\zeta_i^2 - 1})}{2\sqrt{\zeta_i^2 - 1}}\,Q_i^{n+1}$$

$$\frac{3z_{2i}^{n+1} - 4z_{2i}^n + z_{2i}^{n-1}}{2\Delta t} =$$

$$\omega_i(-\zeta_i - \sqrt{\zeta_i^2 - 1})\,z_{2i}^{n+1} + \frac{(\zeta_i + \sqrt{\zeta_i^2 - 1})}{2\sqrt{\zeta_i^2 - 1}}\,Q_i^{n+1} \quad (10)$$

which as in Equation 6 can be integrated to steady-state in pseudo-time. This allows for the inclusion of non-linearities in the structural model. The current version of the code employs a second-order accurate discretization of the time derivative operator. The third-order accurate discretization has been implemented in the three-dimensional version of the program. This pseudo-time integration yields the following equations

$$
\begin{aligned}
\frac{dz_{1i}}{dt^*} + R_{1i}^*(z_{1i}) &= 0 \\
\frac{dz_{2i}}{dt^*} + R_{2i}^*(z_{2i}) &= 0, \qquad (11)
\end{aligned}
$$

where

$$
\begin{aligned}
R_{1i}^*(z_{1i}) &= \left\{ \frac{3}{2\Delta t} - \omega_i(-\zeta_i + \sqrt{\zeta_i^2 - 1}) \right\} z_{1i} \\
&\quad - \frac{(-\zeta_i + \sqrt{\zeta_i^2 - 1})}{2\sqrt{\zeta_i^2 - 1}}\,f_i + S_{1i} \\
R_{2i}^*(z_{2i}) &= \left\{ \frac{3}{2\Delta t} - \omega_i(-\zeta_i - \sqrt{\zeta_i^2 - 1}) \right\} z_{2i} \\
&\quad - \frac{(\zeta_i + \sqrt{\zeta_i^2 - 1})}{2\sqrt{\zeta_i^2 - 1}}\,f_i + S_{2i}
\end{aligned}
$$

and S_{ji} are source terms from the previous iteration levels. Notice that each of Equations 10 is coupled implicitly to the solution of the Euler equations since Q_i contains both C_l and C_m. The pseudo-time integrations will solve this problem as we shall see in the next section. For a given Q_i^{n+1}, Equations 10 can be solved algebraically for the new values of z_{1i} and z_{2i}. The solution of Equations 11 is performed with a four-stage Runge-Kutta scheme in order to provide for the possible future inclusion of non-linearities in the structural model.

Fluid-Structure Coupling

Since the goal is to achieve full convergence of both Equations 5 and 10 simultaneously, a special strategy will be used. The solution for all time levels up to n has been calculated and the flow fields at time levels n and $n-1$ are stored in memory. In order to march the Euler equations forward in time, we will use a number of multigrid cycles that drive Equations 6 to a steady-state. If we took this solution, computed C_l and C_m at time level $n+1$, and then used this information to calculate the new position of the airfoil according to Equations 10, the new position and velocity of the airfoil at $n+1$ will presumably change the flow solution (values of C_l and C_m). As a result, the set of equations will not be fully converged. In order to fully

converge the system, when marching to a steady-state in pseudo-time, the two systems exchange information after every pseudo-time step. We will proceed as follows:

- At time level n, perform a multigrid iteration of the pseudo-time Euler equations (6) and calculate the temporary values of C_l and C_m.

- This information is sent to the structural equations, which determine the approximate position and velocity of the airfoil at the end of the real time step.

- The new position and velocity of the section are taken into account by the flow equations which repeat the process.

It is found that after 7 to 10 iterations of the previous cycle, the solution is fully converged—we have marched the two sets of equations forward in time one real time step Δt. In practice it is found that a minimum of two multigrid cycles in pseudo-time are necessary before the exchange of information with the structural equations of motion.

Results and Discussion

Results were computed with the coupled algorithm described above for a two-dimensional swept wing model (Case A of Isogai). The structural parameters for this case are: $x_\alpha = 1.8$, $r_\alpha^2 = 3.48$, $a = -2.0$, $\omega_h = 100$ rad/sec, $\omega_\alpha = 100$ rad/sec, and $\mu = 60$. Notice that the pivot point lies ahead of the leading edge of the airfoil in question. The airfoil cross section is that of the NACA 64A010 taken from.[26] These parameters were empirically chosen by Isogai in order to simulate the behavior of an outboard section of a sweptback wing. The normal modes of vibration of this two-dimensional model closely resemble those of the swept wing, where the plunging mode is the flutter mode at the bottom of the "transonic dip".

In order to validate the unsteady flow code UFLO82, calculations were done on a 160×32 O-mesh. A detail of this mesh can be seen in Figure 2. A NACA 64A010 airfoil section was used at a free stream Mach number $M_\infty = 0.796$, and 36 equal real time steps per period of forced oscillation were taken. The airfoil was forced in pitch about the quarter chord at a reduced frequency of 0.202. Experimental results are taken from.[25] As we can see in Figure 3, the computed results are in extremely good agreement with the experiment, and therefore, confidence is gained for the application of this algorithm to the aeroelastic problem.

Before proceeding to the fully coupled aeroelastic problem, a series of tests were tried on the same grid but using the third- and fourth- order accurate discretizations of the time derivative operator in Equation 2. The third-order accurate discretization yields a considerable improvement over the baseline discretization. As we can see in Figure 4 the computations with the third-order accurate discretization using 12 and 8 steps per period are barely distinguishable from the second order accurate results using 72 steps per period. The third-order accurate algorithm has a storage penalty since one extra level of computations needs to be stored. For Euler flows, this penalty is greatly outweighed by the savings in processor time that result from a maximum CFL number on the order of $12,000$ in the smallest cells of the domain. The third-order accurate discretization has been used in the three-dimensional version of the code. The fourth-order accurate discretization has been found to be unstable with the current treatment of the flow equations.

For aeroelastic problems, initial calculations were done on an O-mesh with 96×16 cells and 36 real time steps per period of forced oscillation. Variations of the results with spatial and time grid refinements are presented later.

In general, the airfoil is forced sinusoidally in pitch about the elastic axis for three complete cycles at a frequency ω_f close to the first mode of vibration of the structure. At the end of these forced cycles, the imaginary pin keeping the airfoil from displacing vertically is removed, and the system is allowed to evolve forced by its own self-induced loads. The response is computed for different Mach numbers and different values of the speed index, V.

For low speed indices, the vibrations are seen to decay with time as can be seen in Figure 5. As V increases the system reaches the neutrally stable point at which self-supported oscillations of constant amplitude appear—this is the flutter point. An example of the this behavior is found in Figure 6. If the speed index is increased any further, the system is unstable and the amplitudes of both the pitching and plunging motions will grow exponentially with time until the structure fails. An example of divergent behavior can be seen in Figure 7. The three cases shown correspond to three different Mach numbers simply for clarity of the solutions, but each of the points on the flutter boundary was computed by varying the speed index while holding the Mach number constant.

When this process is repeated for several Mach numbers a flutter boundary for the given airfoil can be computed. Several runs are needed to compute each point on the boundary until the value of the speed index that yields a zero damping response is found. Isogai's configuration has been the subject of several investigations. Figure 8 shows a comparison of the calculated flutter boundaries from the present code and previous references ([6,9]). As we can see, all of the codes predict fairly well the "transonic dip" phenomenon. The bottom of the dip is placed at a speed index of $V = 0.5332$ by the present code. The transonic small disturbance (TSD) codes deviate less than

10% from this value. The results from TSD codes lie at a higher speed index in the low Mach number range ($M_\infty \sim 0.75 - 0.85$) possibly due to the inadequate prediction of the phase lag in the shock wave motion. As the Mach number approaches unity, both the TSD and the present Euler codes seem to agree more closely, probably due to the fact that the TSD is an exact approximation in the limit $M_\infty \to 1.0$. Disagreement with previous Euler results by Kousen[10] in this range can only be explained by the different spatial meshes used (C-mesh vs. O-mesh in the present calculations).

Multiple flutter points are observed at a range of Mach numbers in the neighborhood of $M_\infty = 0.85$. Once in the unstable region, further increase in the speed index past the second flutter point results in a stable configuration, which will again become unstable for even higher values of V. Right below $M_\infty = 0.9$, a sharp rise in the flutter speed index is observed. For higher values of the Mach number, flutter points exist but occur at higher speed indices. In fact, as we can see in Figure 9, the flutter mode is now the second mode of vibration (with the higher frequency and the antisymmetric mode).

Although the transonic small disturbance codes seem to agree closely with the Euler codes, they can not accurately model all the flow phenomena present in the calculations. The first Euler code used by Bendiksen and Kousen showed the existence of limit cycle behavior[11] in the airfoil response at certain Mach numbers. With the present code, the existence of these limit cycles (a purely non-linear phenomenon) has been confirmed, and will be the subject of further study. As we can see in Figure 10, the amplitude of the vibrations initially increases exponentially until the non-linearities in the aerodynamics *limit* the amplitude of the motion.

Once the validity of the structural integrator has been established, several numerical experiments were conducted in order to assess its performance. Using a baseline case with an O-mesh of 96×16 cells and 144 time steps per period (fine time grid), the flutter boundary for the NACA 64A010 with Isogai's structural parameters was computed. The same calculation was performed on a 96×16 grid with only 36 time steps per period of forced oscillation. As we can see in Figure 11, both flutter boundaries are in very close agreement except at the $M_\infty = 0.9$ point. The explanation for this disagreement is simple. Since the flutter mode at this Mach number is the second mode, the solution had on the order of only 8 time steps per period of oscillation. The solution is then largely underresolved, and thus the loss of accuracy.

Next, a second numerical experiment was carried out in order to investigate the effects of spatial grid refinement. Now a 192×32 cell mesh was used and 36 time steps per period of forced oscillation were taken. The results are in extremely close agreement with the previous two flutter boundary calculations as can be observed in Figure 12, showing that a 96×16 mesh with 36 steps per period is a valid mesh to obtain flutter boundaries for two-dimensional airfoils. As before, there is a problem with the $M_\infty = 0.9$ point due to the same reason explained above.

Finally, the flutter point for $M_\infty = 0.825$ was calculated, but this time we varied the amplitude of the forcing. From Figure 13 we can see that both the flutter speed index and the flutter reduced frequency are practically independent of the amplitude of the forcing motion as opposed to results reported before.[9]

Computer Requirements

The preceding computations were carried out on a Convex C3400 with four processors at Princeton University. For a spatial grid of 192×32 the total CPU time required is on the order of 9.4 sec per time-step. Notice that only about 144 steps are necessary for each run. The performance of the present code, UFLO82S, is one or two orders of magnitude better than the explicit version of the code, depending on the value of the reduced frequency k_c of the response. This is the major advantage of using the implicit discretization vs. an explicit one.

Conclusions and Recommendations

The following conclusions can be drawn from the results of this paper:

1. A procedure to integrate the Euler equations forward in time coupled with a typical section aeroelastic wing model has been developed.

2. Full convergence of the two relevant sets of equations is achieved at *every time* step of the calculation.

3. Proof has been presented that Jameson's fully-implicit multigrid-driven algorithm (^{14}) can be used for aeroelastic analysis with great computational savings.

4. Extension of the described approach to three-dimensional wings is necessary in order to treat practical configurations and to validate the two-dimensional typical section wing model approximation. Efforts to complete this project are already under way.

5. Further refinement of the aerodynamic model (Navier-Stokes) is required in order to validate the Euler and TSD results, and to extend the validity of the model into the separated flow region where additional physical phenomena are present.

Acknowledgements

References

[1]Stevenson, J. R., "Shock-Induced Self-Excited Airfoil Bending Oscillations," Los Angeles Division, Rockwell International, paper presented to the Aerospace Flutter and Dynamics Council, Las Vegas, Nevada, Oct 19-20, 1976.

[2]Isogai, K., "On the Transonic-Dip Mechanism of Flutter of a Sweptback Wing," AIAA Journal, Vol. 17, No. 7, pp. 793-795, July 1979.

[3]Isogai, K., "Transonic Dip Mechanism of Flutter of a Sweptback Wing: Part II," AIAA Journal, Vol. 19, Sept. 1981, pp. 1240-1242.

[4]Rizzetta, D. P., "Time-Dependent Response of a Two-Dimensional Airfoil in Transonic Flow," AIAA Journal, Vol. 17, January 1979.

[5]Borland, C. J., "XTRAN3S-Transonic Steady and Unsteady Aerodynamics for Aeroelastic Applications," Air Force Wright Aeronautical Laboratories, AFWAL-TR-85-3124 Report, January 1986.

[6]Edwards, J. W., *et al.*, "Time-Marching Transonic Flutter Solutions Including Angle of Attack Effects," Journal of Aircraft, Vol. 20, No. 11, November 1983, pp. 899-906.

[7]Ashley, H., "Role of Shocks in the 'Sub-Transonic' Flutter Phenomenon," Journal of Aircraft, Vol. 17, March 1980, pp. 187-197.

[8]Farmer, M.G. and Hanson, P.W., "Comparison of Supercritical and Conventional Wing Flutter Characteristics," Procs. AIAA/ASME/SAE 17th SDM Conference, King of Prussia, Pennsylvania, April 1976, pp. 608-611; see also NASA TM X-72837, May 1976.

[9]Bendiksen, O. O. and Kousen, K. A., "Transonic Flutter Analysis Using the Euler Equations," AIAA Paper 87-0911-CP, AIAA Dynamics Specialists Conference, Monterey, California, April 1987.

[10]Kousen, K. A., "Non-Linear Phenomena in Computational Transonic Aeroelasticity," Ph.D. Dissertation, Dept. of Mechanical and Aerospace Engineering, Princeton University, January 1989.

[11]Kousen, K. A. and Bendiksen, O. O., "Nonlinear Aspects of the Transonic Aeroelastic Stability Problem," AIAA Paper No. 88-2306, presented at the AIAA/ASME/ASCE/AHS 29th Structures, Structural Dynamics, and Materials Conference, Williamsburg, Virginia, April 1988 .

[12]Guruswamy, G. P., "Unsteady Aerodynamic and Aeroelastic Calculations for Wings Using Euler Equations," AIAA Journal, Vol. 28, No. 3, March 1990.

[13]Guruswamy, G. P., "Vortical Flow Computations on Swept Flexible Wings Using Navier-Stokes Equations," AIAA Journal, Vol. 28, No. 12, December 1990.

[14]Jameson, A., "Time Dependent Calculations Using Multigrid, with Applications to Unsteady Flows Past Airfoils and Wings," AIAA Paper 91-1596, June 1991.

[15]Jeltsch, R., "Stability on the Imaginary Axis and A Stability of Linear Multistep Methods," BIT, Vol. 18, 1978, pp. 170-174 .

[16]Gear, C. W., "Numerical Initial Value Problems in Ordinary Differential Equations," Prentice Hall, Englewood Cliffs, New Jersey, 1971.

[17]Melson, N. D., Sanetrik, M. D., and Atkins, H. L.,"Time-Accurate Navier-Stokes Calculations with Multigrid Acceleration", Procs. of the Sixth Copper Mountain Conference on Multigrid Methods, Copper Mountain, Colorado, April, 1993.

[18]Arnone, A., Liou, M. S., and Povinelli, L. A., "Multigrid Time-Accurate Integrations of Navier-Stokes Equations," 24th Fluid Dynamics Conference, July 1993, Orlando, Florida, AIAA Paper 93-3361.

[19]Jameson, A., "Solution of the Euler Equations by a Multigrid Method," Applied Mathematics and Computation, Vol. 13, pp. 327-356, 1983.

[20]Rizzi, A.,"Numerical Implementation of Solid-Body Boundary Conditions for the Euler Equations," ZAMM, vol. 58, pp. 301-304, 1978.

[21]Venkatakrishnan, V.,"Computation of Unsteady Transonic Flows over Moving Airfoils," Ph.D. Dissertation, Dept. of Mechanical and Aerospace Engineering, Princeton University, October 1986.

[22]Bisplinghoff, R. L., Ashley, H. and Halfman, R. L., Aeroelasticity, Addison-Wesley, Reading, Massachusetts, 1955.

[23]Dowell, E. H., Curtiss, H. C., Scanlan, R. H. and Sisto, F., A Modern Course in Aeroelasticity, Sijthoff and Noordhoff, Alphen ann den Rijn, The Netherlands, 1978.

[24]Bathe, K. J., "Finite Element Procedures in Engineering Analysis," Prentice Hall, Englewood Cliffs, New Jersey, 1982.

[25]Davis, S. S., "NACA 64 A010 (NASA Ames Model) Oscillatory Pitching," in Compendium of Unsteady Aerodynamic Measurements, AGARD Report No. 702, August 1982.

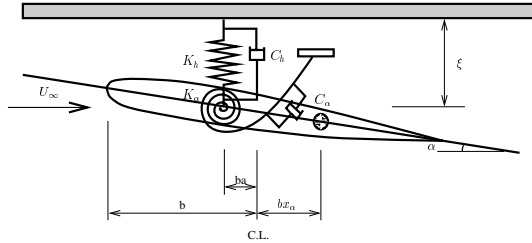[26]Bland, S. R., "AGARD Two-Dimensional Aeroelastic Configurations," AGARD Report No. 156, August 1979.

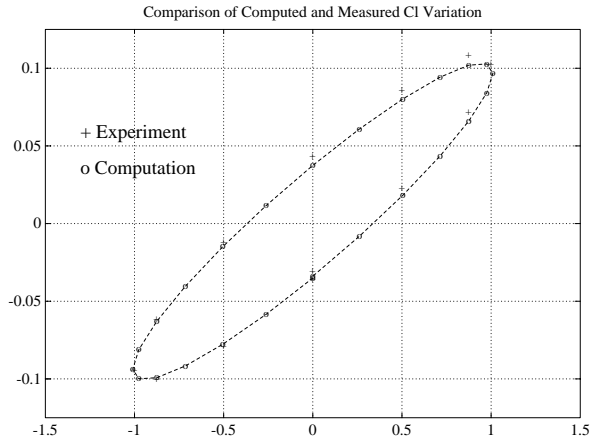**Fig. 1   Typical Section Wing Model Geometry and Parameters.**

Fig. 3   Comparison of Calculated and Experimental Results [25].
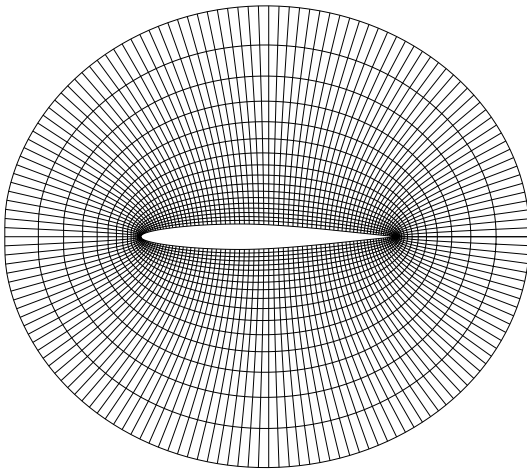

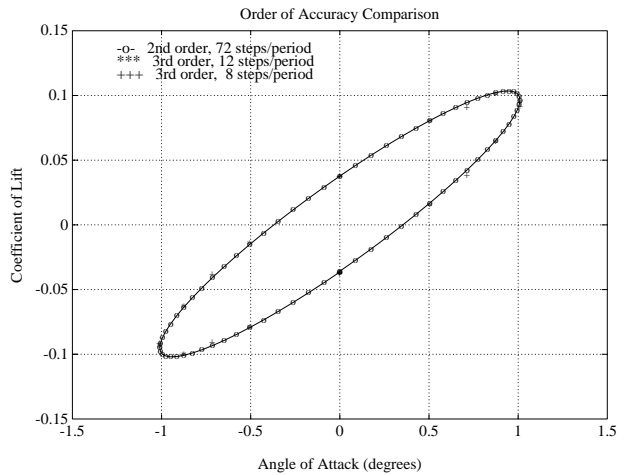**Fig. 2   Detail of the O-Mesh Used in Calculations.**

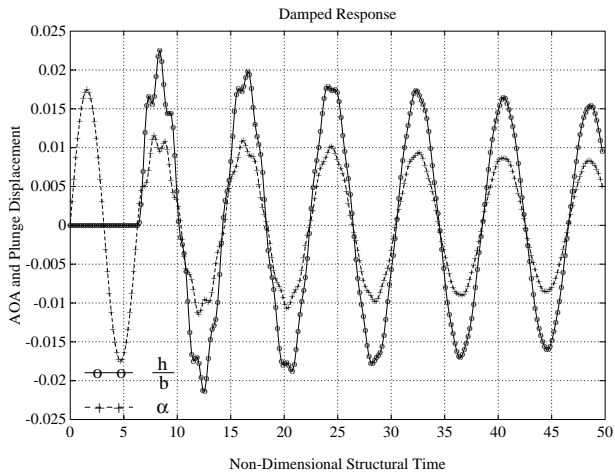**Fig. 4   Comparison between Second- and Third-Order Accurate Calculations.**

Fig. 5   Damped Response. $M_\infty = 0.85$, $V_f = 0.439$, $\Delta\alpha = 1.0°$, $\omega_f = 100\,\mathrm{rad/sec}$.
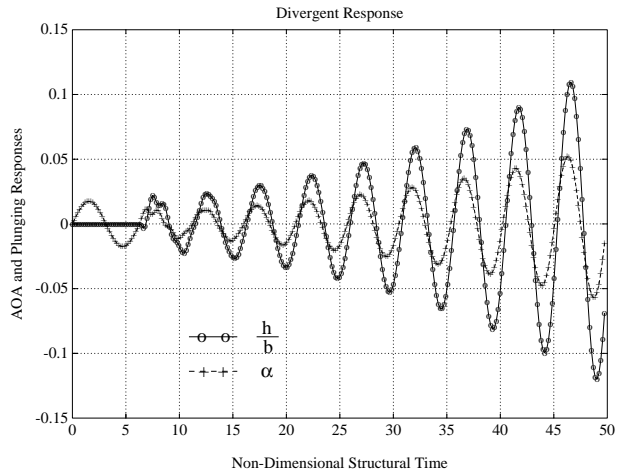

Fig. 7   Divergent Response. $M_\infty = 0.875$, $V_f = 1.420$, $\Delta\alpha = 1.0°$, $\omega_f = 100\,\mathrm{rad/sec}$.
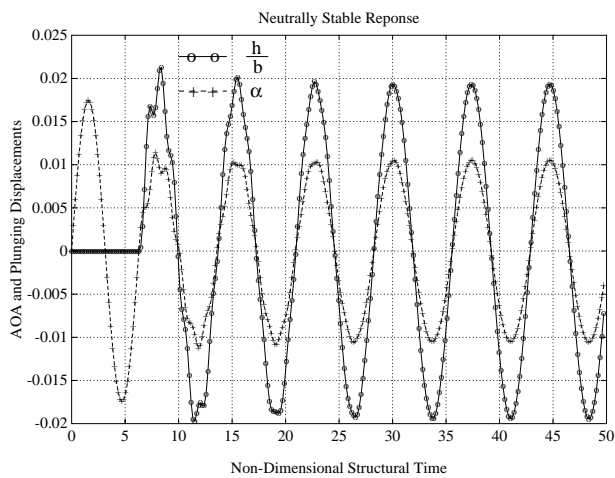
Fig. 6   Neutral Response. $M_\infty = 0.825$, $V_f = 0.612$, $\Delta\alpha = 1.0°$, $\omega_f = 100\,\mathrm{rad/sec}$.
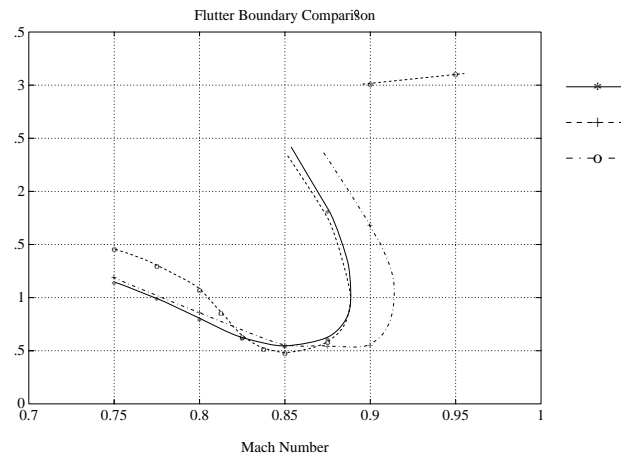
Fig. 8   Flutter Boundary Comparison. Present code and references [6] and [10].
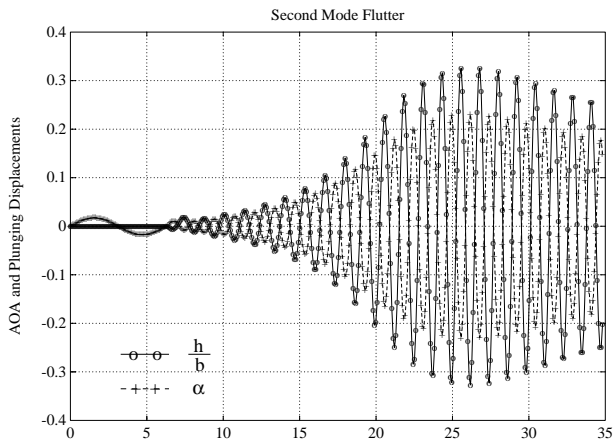
Fig. 9 Second Mode Response. $M_\infty = 0.900$, $V_f = 2.840$, $\Delta\alpha = 1.0°$, $\omega_f = 100\,\mathrm{rad/sec}$.
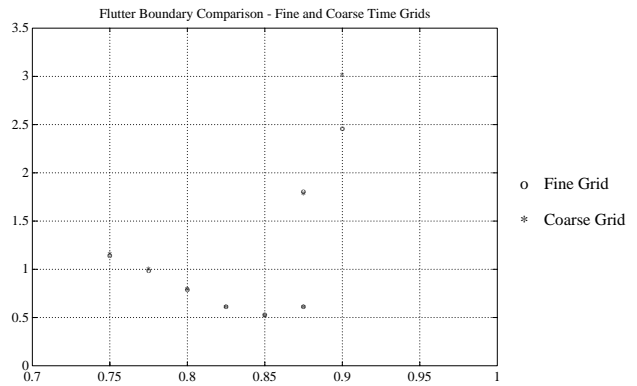
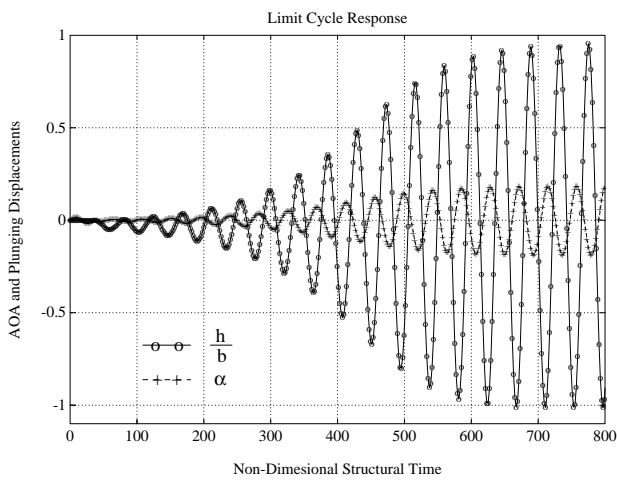Fig. 11 Time Grid Flutter Boundary Comparison. Fine Grid: 144 steps/period. Coarse Grid: 36 steps/period.

Fig. 10 Limit Cycle Response. $M_\infty = 0.75$, $V_f = 1.320$, $\Delta\alpha = 1.0°$, $\omega_f = 100\,\mathrm{rad/sec}$.
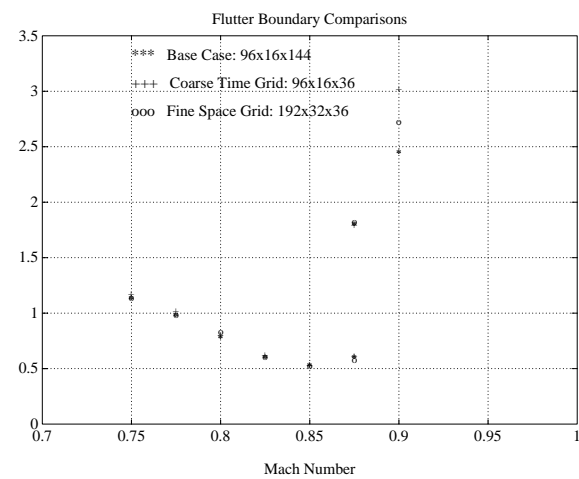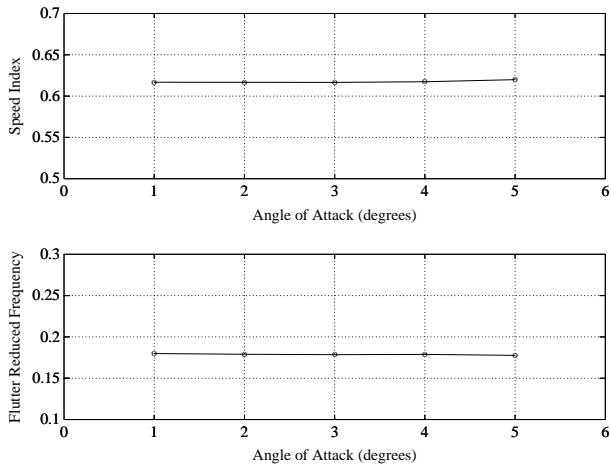

Fig. 12 Spatial Grid Refinement Comparison.

Fig. 13   Flutter Parameters Dependence on Forcing Amplitude, $M_\infty = 0.825$.